Nano Research

ISSN 1998-0124 CN 11-5974/O4
https://doi.org/10.26599/NR.2026.94908860

Research Article

A highly linear and durable flexible strain sensor based on MoS_2 van der Waals films for soft machines

Xiangxu Zhu[1,2], Hao Ouyang[1,2], Liangjing Shi[1], Yin Cheng[1], Jing Sun[1], Ranran Wang[1,3](✉)

[1] The State Key Laboratory of High Performance Ceramics, Shanghai Institute of Ceramics, Chinese Academy of Sciences, Shanghai 200050, China

[2] Center of Materials Science and Optoelectronics Engineering, University of Chinese Academy of Sciences, Beijing 100049, China

[3] School of Chemistry and Materials Science, Hangzhou Institute for Advanced Study, University of Chinese Academy of Sciences, Hangzhou 310024, China

Nano Res., **Just Accepted Manuscript** • https://doi.org/10.26599/NR.2026.94908860
https://www.sciopen.com/journal/1998-0124 on May. 21, 2026

© The Authors(s)

Just Accepted

This is a "Just Accepted" manuscript, which has been examined by the peer-review process and has been accepted for publication. A "Just Accepted" manuscript is published online shortly after its acceptance,which is prior to technical editing and formatting and author proofing. Tsinghua University Press (TUP) provides "Just Accepted" as an optional and free service which allows authors to make their results available to the research community as soon as possible after acceptance. After a manuscript has been technically edited and formatted, and the page proofs have been corrected, it will be removed from the "Just Accepted" web site and published officially with volume and article number (e.g., *Nano Research*, **2025**, *18*, 94906990). Please note that technical editing may introduce minor changes to the manuscript text and/or graphics which may affect the content, and all legal disclaimers that apply to the journal pertain. In no event shall TUP be held responsible for errors or consequences arising from the use of any information contained in these "Just Accepted" manuscripts. To cite this anuscript please use its Digital Object Identifier (DOI®),which is identical for all formats of publication.

Just Accepted

TABLE OF CONTENTS (TOC)

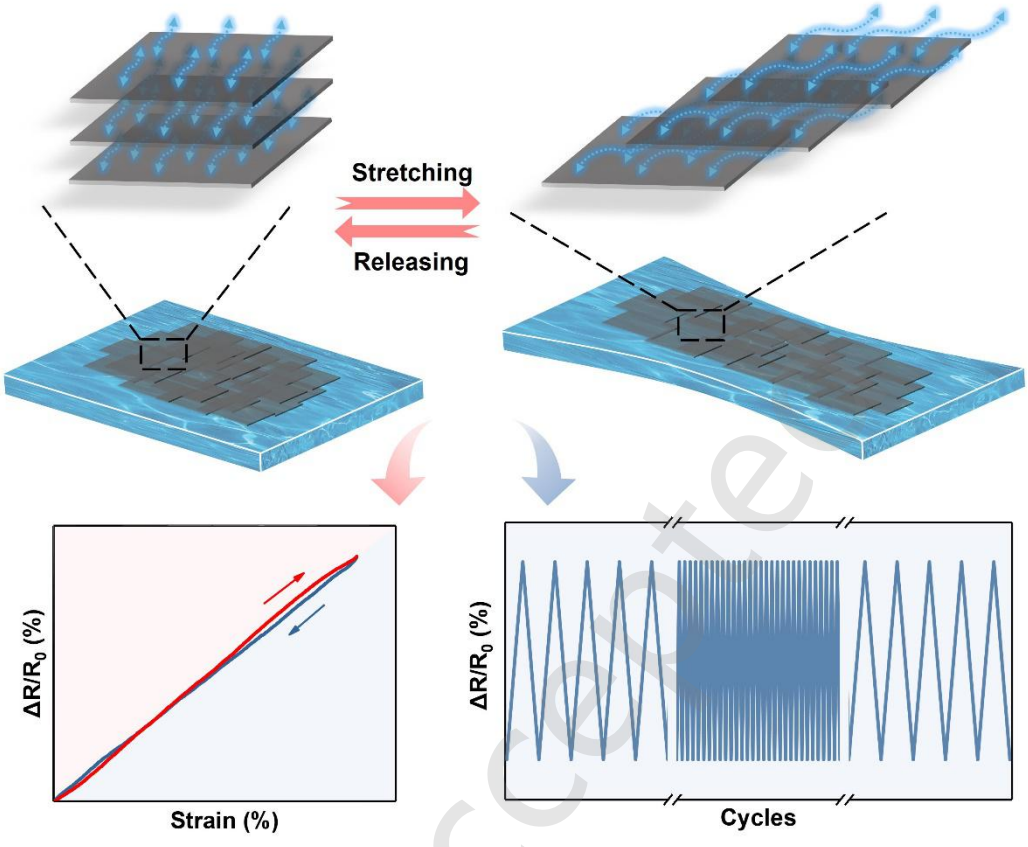

A MoS_2 van der Waals film strain sensor leverages reversible interlayer sliding to deliver high linearity (R^2 = 0.999), low hysteresis, and high durability (>40,000 cycles), overcoming limitations of crack-based sensors. Its reliable performance enables precise soft machine applications, such as deformation monitoring and slip detection in a flexible gripper.

Just Accepted

Nano Research

Open Access

Research Article

A highly linear and durable flexible strain sensor based on MoS_2 van der Waals films for soft machines

Xiangxu Zhu[1,2], Hao Ouyang[1,2], Liangjing Shi[1], Yin Cheng[1], Jing Sun[1], and Ranran Wang[1,3]

[1] *The State Key Laboratory of High Performance Ceramics, Shanghai Institute of Ceramics, Chinese Academy of Sciences, Shanghai 200050, China*

[2] *Center of Materials Science and Optoelectronics Engineering, University of Chinese Academy of Sciences, Beijing 100049, China*

[3] *School of Chemistry and Materials Science, Hangzhou Institute for Advanced Study, University of Chinese Academy of Sciences, Hangzhou 310024, China*

Received: 5 March 2026; **Revised:** 13 May 2026; **Accepted:** 21 May 2026

Address correspondence to wangranran@mail.sic.ac.cn

Cite this article: *Nano Research*, 2026, 19, 94908860 https://doi.org/10.26599/NR.2026.94908860

ABSTRACT: Flexible strain sensors for soft and deformable mechanical systems are required to deliver high linearity and durability under repeated deformation, which remain challenging for crack-based sensing mechanisms. Here, we report a highly linear and durable flexible strain sensor based on molybdenum disulfide (MoS_2) van der Waals films. MoS_2 nanosheets were prepared via electrochemical intercalation exfoliation and assembled into conductive films dominated by interlayer van der Waals interactions, followed by surface treatment to enable strong bonding with a polydimethylsiloxane (PDMS) substrate. Benefiting from a reversible interlayer sliding dominated sensing mechanism, the sensor exhibits high linearity (R^2 = 0.999) over a wide strain range, low hysteresis, fast response and recovery behavior, and excellent durability exceeding 40,000 loading–unloading cycles. Furthermore, the sensor shows reliable response under the temperature range from −20 °C to 80 °C, ensuring its applicability across different scenarios. As a representative demonstration, the sensor is integrated onto a flexible gripper to enable deformation monitoring and slip state discrimination. These results highlight the potential of interlayer sliding based strain sensors for advanced soft machine related applications.

KEYWORDS: flexible strain sensor, MoS_2 van der Waals films, interlayer sliding, durability, soft machines

Just Accepted

1 Introduction

In recent years, driven by the rapid development of emerging information technologies such as big data, artificial intelligence, and the Internet of Things, electronic devices have been accelerating toward flexible, wearable, and intelligent architectures[1]. As core components for information perception and interaction, flexible sensors have demonstrated broad application prospects in healthcare monitoring[2-5], human–machine interfaces[6, 7], and deformable mechanical systems[8, 9].

In practical applications involving soft and deformable mechanical structures, such as soft grippers and soft robots, flexible strain sensors are not only responsible for detecting structural deformation but also play critical roles in state recognition, closed-loop control, and motion feedback[10, 11]. These application scenarios impose stringent requirements on sensing linearity, signal fidelity, and long term operational durability under repeated deformation[12, 13]. Consequently, the development of flexible strain sensors capable of delivering stable, repeatable, and quantitatively reliable signals under cyclic loading has become a key pathway toward advanced intelligent flexible systems.

Among various types of flexible sensors, resistive strain sensors have attracted extensive attention due to their simple device configuration, mature fabrication processes, and stable electrical signals that are easy to acquire and process[14, 15]. Their working principle relies on converting external mechanical strain into measurable resistance variations through deformation-induced changes in conductive networks[16]. However, conventional bulk metallic or semiconducting conductive materials generally suffer from limited ductility, intrinsic brittleness, and poor fatigue resistance, which severely restrict their applicability in flexible devices subjected to large deformations and repeated loading cycles[17, 18]. To overcome these limitations, increasing research efforts have been devoted to low-dimensional conductive materials, such as carbon nanotubes[19, 20], graphene[21-24], MXenes[25-27], and metallic nanowires[28-30], which are commonly integrated with elastomeric substrates (e.g., PDMS, Ecoflex, or TPU) to construct stretchable flexible strain sensors. At the initial stage of stretching, the adjacent structural units of the low-dimensional materials can undergo relative sliding. However, owing to strong interfacial interactions such as hydrogen bonding, physical entanglement, or junction welding in common low-dimensional materials, the interunit sliding process is often constrained. As strain continues to increase, stress concentration accumulates locally, eventually leading to crack initiation and propagation, even rupture of conductive pathways.[31] Consequently, most reported resistive flexible strain sensors operate based on crack-dominated sensing mechanism. Although such crack

formation can effectively amplify resistance variation and improve strain sensitivity, the random initiation and evolution of cracks during stretching often lead to segmented or nonlinear electrical responses, thereby compromising quantitative accuracy and repeatability. For example, Lee et al.[32] developed a laser-induced graphene–based strain sensor fabricated via ZnO nanoparticle-assisted photothermal enhancement, in which microcracks were generated and propagated during stretching. The gauge factor (GF) increases from approximately 146 at 4% strain to 1214 at 10% strain, accompanied by a distinctly nonlinear and piecewise resistance–strain relationship. Yang et al.[33] reported a MXene strain sensor modulated by Ag-thiolate interactions to control the crack structure, which exhibits a significant nonlinear resistance–strain response. Moreover, cracks are typically difficult to fully recover during repeated loading–unloading cycles, which results in irreversible structural damage in conductive layers, increased hysteresis, and degradation of cycling stability.[25, 34] These issues have become major bottlenecks for the long term reliable operation of high-performance flexible strain sensors.

In contrast, strain response mechanisms dominated by interlayer sliding provide an alternative strategy to address these challenges.[35] By transforming macroscopic mechanical deformation into relative sliding between microscopic conductive units, interlayer sliding effectively alleviates stress concentration within conductive layers and suppresses crack initiation and propagation[36]. This mechanism enables continuous, reversible, and highly linear resistance responses while mitigating material fatigue and structural degradation, offering a promising route toward high-precision and durable flexible strain sensors.[37]

To realize such a sliding-dominated sensing mechanism, the choice of conductive material is of critical importance. Recent studies have shown that certain inorganic semiconductors can exhibit pronounced plastic deformation enabled by crystallographic slip or interlayer sliding.[38] However, plastic deformation in inorganic semiconductors that relies on defect-mediated dislocation motion or lattice rearrangement often exhibits irreversible electrical behavior under mechanical deformation.[39] Metallic nanowire networks may also allow relative sliding in the absence of junction welding, but their high aspect ratios result in limited changes in conductive pathway geometry under strain, leading to small resistance variation and limited sensitivity.[40] In this context, layered van der Waals semiconductors exhibit distinct advantages.[41] Among them, molybdenum disulfide (MoS_2), a representative layered transition metal dichalcogenide, has been experimentally demonstrated to sustain deformation dominated by interlayer sliding rather than brittle fracture.[42] MoS_2 nanosheets can be readily produced via scalable solution-based exfoliation and assembled into large-area van der Waals thin films.[43] Owing to weak interlayer van der Waals interactions, such films enable reversible interlayer sliding under applied strain.[44] As a result, MoS_2 van der Waals thin films can accommodate large mechanical deformation without fracture, endowing flexible strain sensors with continuous, highly linear resistance responses, enhanced durability, and excellent structural stability under cyclic loading.

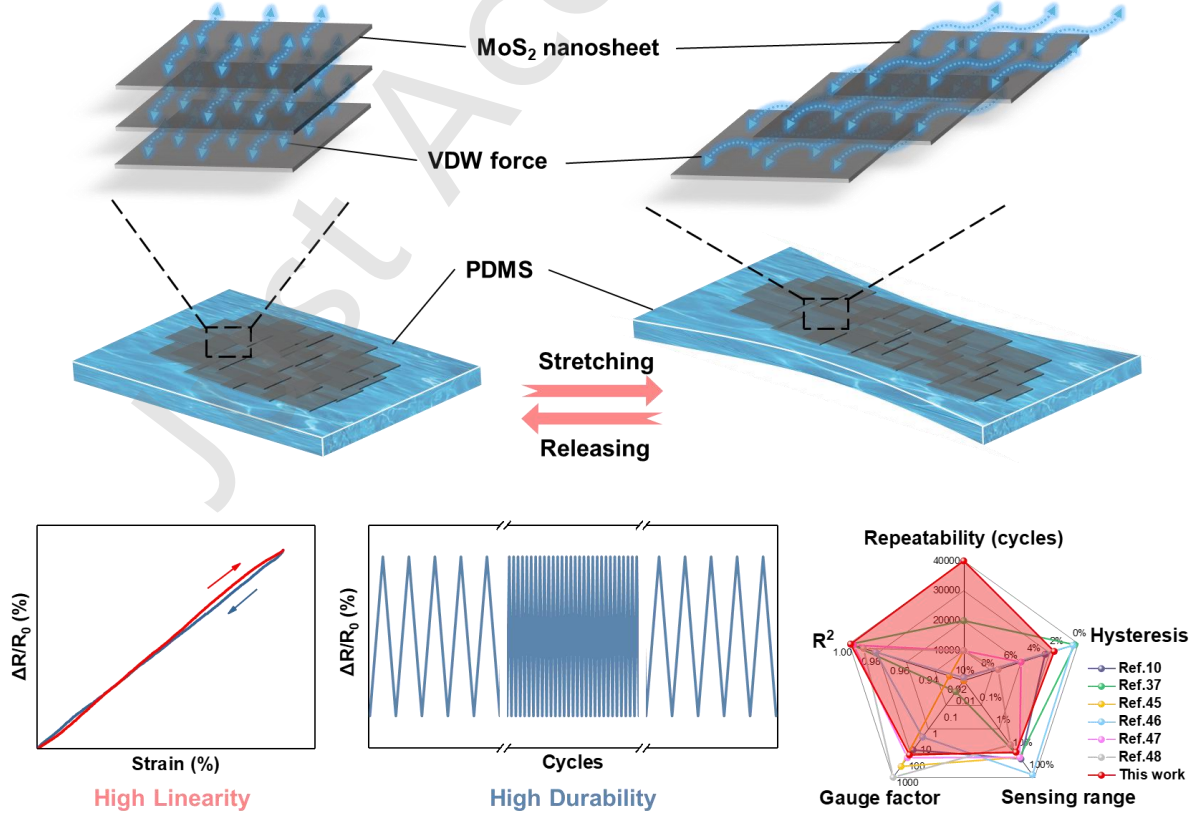

Figure 1 Design concept and overall performance of the flexible strain sensor based on MoS_2 van der Waals films.

Herein, we report a crack-free flexible strain sensor based on MoS_2 van der Waals films (as shown in Figure 1). MoS_2 crystals were exfoliated via an electrochemical intercalation approach to obtain conductive thin films without interlayer chemical

Just Accepted

bonding, in which the nanosheets are assembled through van der Waals interactions. After surface treatment by oxygen plasma, the films were integrated with a PDMS substrate through a facile transfer process to construct flexible strain sensors. Distinct from crack-based sensing mechanisms, the strain response of the proposed sensor is governed by reversible interlayer sliding, which results in a highly linear and stable electromechanical behavior with effectively suppressed hysteresis under repeated deformation. Moreover, compared to the recently published result,[10, 37, 45-48] our strain sensor achieves a favorable balance among key sensing metrics, including gauge factor, sensing range, linearity, hysteresis, and repeatability (Table S1 in the ESM). More importantly, this work establishes interlayer sliding as a core sensing paradigm, which provides a generalizable design principle for realizing highly linear and durable flexible strain sensors. Leveraging this comprehensive sensing performance, the sensor was further integrated into a flexible gripper, which enables reliable identification of grasping states and accurate discrimination of objects with different sizes. These results demonstrate the promising potential of the proposed flexible strain sensor in soft mechanical systems and suggest its applicability in future soft robot-related applications.

2 Results and discussion

2.1 Structural and Electrical Characterization

We fabricated the strain sensor using a facile method, as shown in Figure S1 in the Electronic Supplementary Material (ESM). The nanosheets were prepared via electrochemical intercalation exfoliation, with the crystals expanding and being loosely structured (Figure S2 in the ESM). Figure 2a shows the transmission electron microscopy (TEM) image of an individual MoS_2 nanosheet. The relatively low contrast indicates its ultrathin nature. The high-resolution TEM image in Figure 2b reveals clear lattice fringes with an interplanar spacing of 0.28 nm, corresponding to the (100) plane of 2H-MoS_2. The inset selected area electron diffraction (SAED) pattern displays hexagonally symmetric diffraction spots indexed to the (100) and (110) planes, confirming the preserved 2H crystalline phase of the exfoliated nanosheets. These results are further corroborated by UV–vis absorption (Figure S3 in the ESM). Atomic force microscopy (AFM) characterization (Figure 2c) shows that the MoS_2 nanosheets possess an average thickness of approximately 4 nm, corresponding to a few-layer structure.

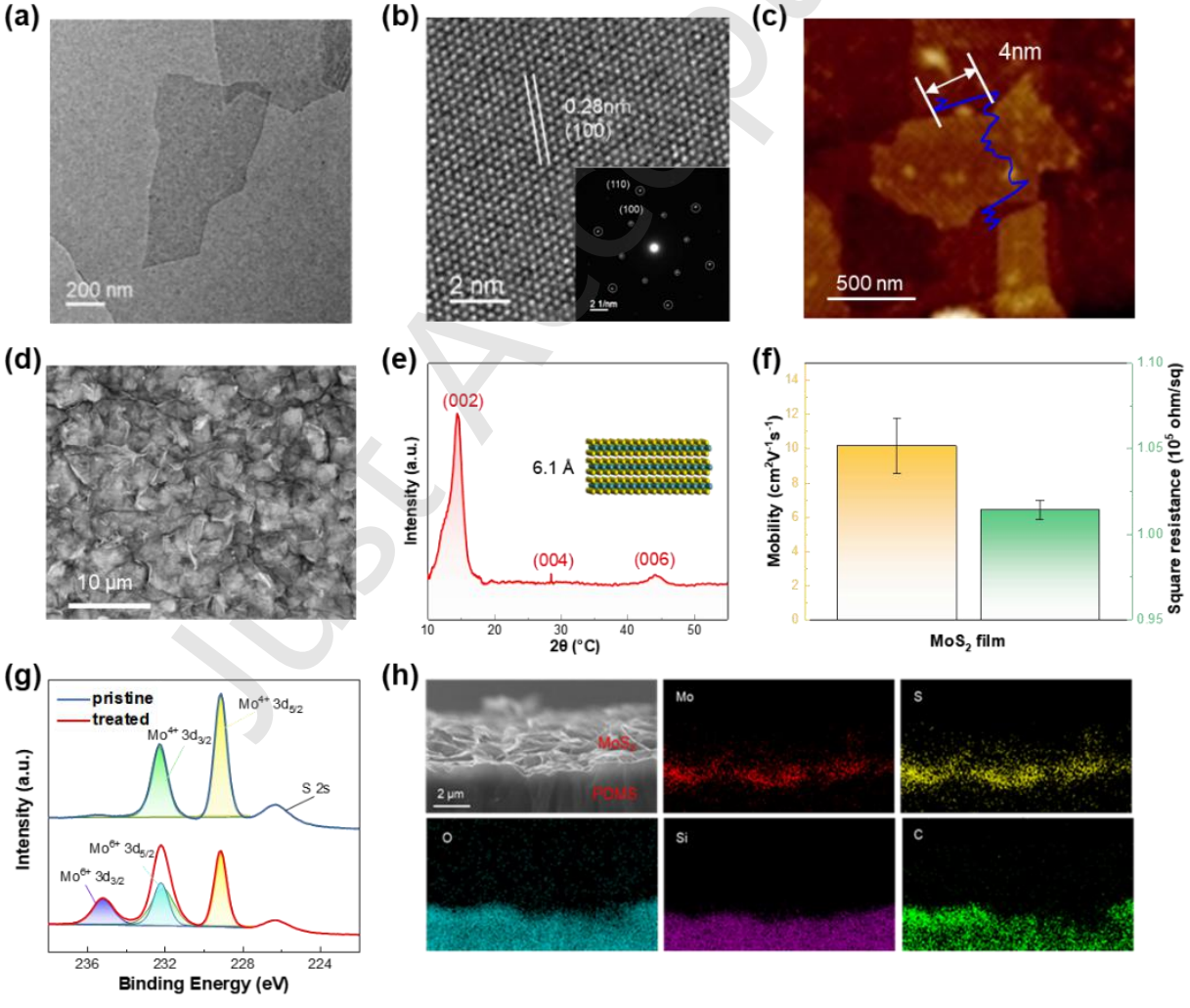

Figure 2 Structural and interfacial characterization of MoS_2 sensing layers. (a) TEM image of an exfoliated MoS_2 nanosheet. (b) High-resolution TEM of the MoS_2 nanosheet, the inset shows the SAED pattern. (c) AFM image and height profile of a MoS_2 nanosheet with an average thickness of ~4 nm. (d) SEM image of the MoS_2 thin film. (e) XRD pattern exhibiting a pronounced (002) peak with an interlayer spacing of ~6.1 Å. (f) Mobility and square resistance of the MoS_2 thin film. (g) XPS spectra and elemental analysis comparing pristine and plasma-treated MoS_2. (h) Cross-sectional SEM image and corresponding EDS elemental mappings of the MoS_2/PDMS composite.

Uniform and crack-free MoS_2 thin films were subsequently fabricated via vacuum filtration. The scanning electron

Just Accepted

microscopy (SEM) image in Figure 2d reveals a dense and continuous stacked nanosheet morphology, indicative of effective film formation. The X-ray diffraction (XRD) pattern of the MoS_2 film (Figure 2e) exhibits a pronounced (002) diffraction peak, from which an interlayer spacing of ~6.1 Å is derived, close to that of pristine bulk MoS_2. This result indicates the absence of interlayer covalent bonding and confirms that the nanosheets are predominantly assembled through van der Waals interactions. Electrical characterization (Figure 2f) shows that the film possesses a sheet resistance of approximately 1.01 × 10^5 Ω sq^{-1} and a carrier mobility of ~10.16 cm^2 V^{-1} s^{-1}, comparable to values reported for individual MoS_2 nanosheets, suggesting that interlayer charge transport is not significantly hindered.

To enhance interfacial coupling with the elastomeric substrate, the MoS_2 film was subjected to oxygen plasma surface treatment. As shown in Figure 2g and Figure S4 in the ESM, X-ray photoelectron spectroscopy (XPS) analysis was performed on the pristine and treated film surfaces. The peaks of Mo 3d can be divided into Mo^{4+} $3d_{3/2}$ (232.3 eV) / Mo^{4+} $3d_{5/2}$ (229.1 eV) and Mo^{6+} $3d_{3/2}$ (235.2 eV) / Mo^{6+} $3d_{5/2}$ (232.2 eV).[49] After the treatment, the Mo^{6+} peak emerged, while S 2s peak decreased and O 1s peak increased. Moreover, XPS combined with argon ion etching was used to characterize the treated film surfaces. The tests shown in Figure S5 in the ESM indicate that the Mo^{6+} peak weakened as the etch depth increased. The above results demonstrate the formation of an oxidized surface layer with a thickness of approximately 5–7 nm and the introduction of abundant oxygen-containing functional groups. This modification effectively converts the weak van der Waals interaction between the MoS_2 film and PDMS into strong interfacial bonding. It should be emphasized that the treatment is limited to the film surface and does not extend into the bulk of the film, thus preserving the intrinsic van der Waals interactions that govern the overall film structure. In addition, cross-sectional SEM and elemental mapping images (Figure 2h) further confirm a compact, void-free interface, indicative of robust interfacial integration.

2.2 Sensing Performance Analysis

The sensing performance of the MoS_2-based strain sensors was then evaluated. Figure 3a shows the relative resistance change ($\Delta R/R_0$) of the sensors as a function of applied tensile strain. The gauge factor (GF), which reflects the sensitivity of the strain sensor, is defined as the slope of the $\Delta R/R_0$–strain curve[50]:

$$GF = \frac{\Delta R/R_0}{\varepsilon} \#(1)$$

where R_0 is the initial resistance and ΔR is the change in resistance under applied strain. As shown in Figure 3a, sensors fabricated from MoS_2 nanosheets obtained under different processing conditions exhibit distinct sensitivities and linear sensing ranges. Specifically, the d_{5min}-c_{1-3k}-MoS_2, d_{10min}-c_{3-5k}-MoS_2, and d_{30min}-c_{5-8k}-MoS_2 sensors (where d denotes the ultrasonication time and c denotes the centrifugation speed range) show GF values of 1.85 (0–30%), 7.19 (0–24.1%), and 40.87 (0–10.8%), respectively. With increasing ultrasonication time and centrifugation speed, the lateral size of the nanosheets decreases from 1.55 μm to 0.52 μm (Figure S6 in the ESM), leading to enhanced sensitivity but a reduced detectable strain range. To balance sensitivity and stretchability, MoS_2 nanosheets with an intermediate lateral size of approximately 800 nm (d_{10min}-c_{3-5k}-MoS_2) were selected for subsequent studies, while the sensor exhibited the highest linearity (R^2 = 0.999). After fixing the lateral size of the MoS_2 nanosheets, the effect of film thickness on sensing performance was investigated. The film thickness was tuned by varying the deposited mass during vacuum filtration. As the filtration volume at a fixed concentration increased from 5 mL to 15 mL, the sensitivity of the strain sensor gradually decreased, whereas the linear sensing range expanded (Figure S7 in the ESM). This trend can be attributed to the increased number of parallel conductive pathways and the suppressed interlayer sliding in thicker films. An intermediate film thickness at a filtration volume of 10 mL provides a balanced combination of sensitivity and stretchability and was therefore selected for subsequent device fabrication.

Beyond sensitivity and linear sensing range, hysteresis is another critical parameter for flexible strain sensors, especially for applications requiring accurate quantitative strain analysis and long-term cyclic operation. The hysteresis phenomenon describes the difference of electrical signal output in flexible sensors at same strain during loading and unloading, which limits measurement accuracy and repeatability in real-time sensing systems. Therefore, low hysteresis is essential for ensuring reliable and stable signal output. To quantitatively evaluate the hysteresis behavior of the strain sensors, the degree of hysteresis (DH) is introduced and defined as[50, 51]:

$$DH = \frac{A_{\text{stretching}} - A_{\text{releasing}}}{A_{\text{stretching}}} \times 100\% \#(2)$$

where $A_{\text{stretching}}$ and $A_{\text{releasing}}$ denote the areas enclosed by the stretching and releasing curves, respectively. A lower DH value corresponds to weaker hysteresis and better reversibility of the electrical response. As shown in Figure 3b, the interfacially treated sensor exhibits nearly overlapping stretching–releasing trajectories with a low hysteresis (DH = 2.10%), indicating highly reversible electromechanical behavior. In contrast, the untreated sensor displays pronounced hysteresis (DH = 26.72%), together with lower
sensitivity (GF = 5.15) and inferior linearity (R^2 = 0.993), which can be attributed to irreversible deformation induced by interfacial mismatch. These results highlight the critical role of interfacial optimization in suppressing hysteresis and enhancing signal reversibility.

Moreover, the sensor exhibits a minimum detectable limit of 0.1% (Figure S8 in the ESM), highlighting its ability to resolve small strains. As shown in Figure 3c, the sensor exhibits a stable electrical response with good symmetry under step-strain loading. The applied tensile strain is increased stepwise from 0% to 15% and subsequently released back to 0% with identical strain increments. During both the loading and unloading processes, the resistance responses corresponding to the same strain levels remain nearly unchanged. This highly symmetric stepwise response indicates excellent reversibility of the sensor within the tested strain range. Under a rapid strain of 0.25%, the response and recovery times are 100 ms and 90 ms, respectively (Figure 3d), confirming fast electromechanical response characteristics. Furthermore, stable resistance responses are observed under various applied strain and loading frequencies. As shown in Figure 3e, the sensor exhibits highly repeatable resistance responses under different strains. As the strain increases, the corresponding

Just Accepted

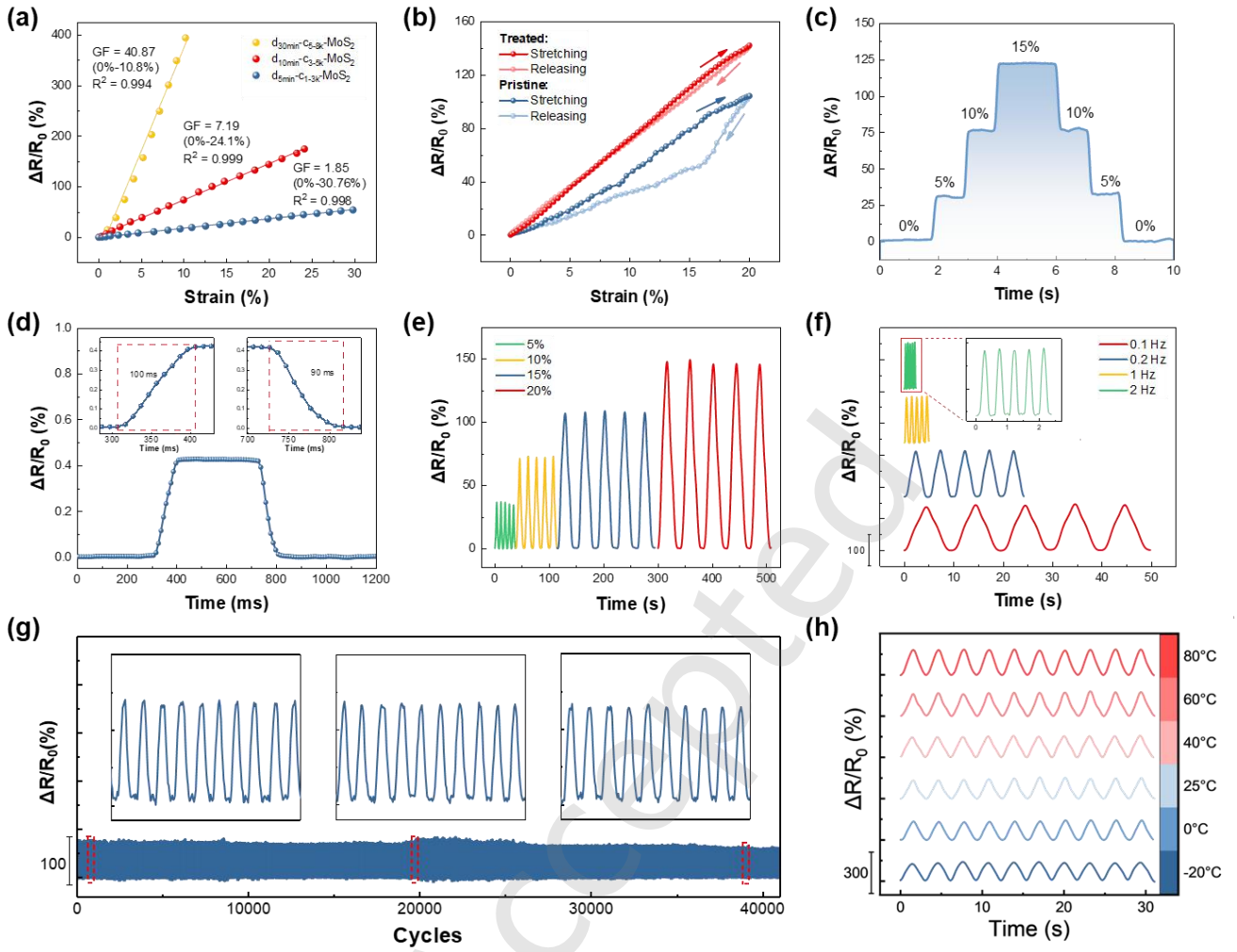

Figure 3 Electromechanical sensing performance of the flexible strain sensor based on MoS_2 van der Waals films. (a) Relative resistance change as a function of applied tensile strain. (b) Stretching and releasing curves of interfacially treated and untreated sensors. (c) Stepwise strain response under incremental tensile deformation. (d) Response and recovery behavior under a small applied strain. (e) Relative resistance responses under different applied strain. (f) Relative resistance responses under different loading frequencies (ε = 20%). (g) Cyclic loading–unloading stability over repeated deformation (ε = 10%). (h) Resistance response under different ambient temperatures (ε = 20%).

relative resistance change increases proportionally, while the response waveforms remain regular and stable. Figure 3f presents the relative resistance change responses of the sensor under a constant strain of 10% at different frequencies ranging from 0.1 to 2 Hz, which shows consistent amplitudes and well-defined waveforms. These results indicate that the sensor maintains a robust and clearly distinguishable electromechanical response over a wide range of strains and loading frequencies.

Cyclic tests (Figure 3g) further demonstrate the excellent mechanical robustness and electrical stability of our strain sensor. Under continuous loading–unloading cycles, the sensor maintains a highly stable relative resistance signal over more than 40,000 cycles without observable performance degradation, indicating that the conductive network and interfacial structure remain intact under repeated mechanical deformation. Notably, such an ultrahigh cycling endurance underscores the exceptional durability of the sensor under repeated mechanical deformation, which is essential for long-term operation in soft machines and wearable applications. For comparison, the cyclic stability of the untreated sensor was also evaluated under the same strain (Figure S9 in the ESM). In contrast to the interfacially treated sensor, the untreated sensor exhibits a pronounced degradation in cyclic stability, characterized by a progressively reduced resistance change amplitude and increased signal fluctuations during repeated loading–unloading cycles. This behavior can be attributed to the insufficient interfacial adhesion between the conductive layer and the substrate, which leads to irreversible interlayer sliding and loss of effective conductive pathways. These results demonstrate that interfacial optimization plays a critical role in enhancing the cyclic stability and signal repeatability of the strain sensor. In addition, the strain sensor maintains reliable operation over a temperature range from −20 °C to 80 °C (Figure 3h), indicating good environmental adaptability. The minor difference in the amplitude of resistance change is mainly attributed to the combined effects of MoS_2's negative temperature coefficient of resistance and the thermal expansion of PDMS.[52] To further investigate the thermal robustness of the sensor, temperature cycling tests were conducted by alternating the temperature between −20 °C and room temperature 25 °C. As shown in Figure S10 in the ESM, the sensor exhibits stable and repeatable resistance responses over multiple temperature cycles. This result indicates that the sensing performance is not significantly affected by temperature variations within this range.

Just Accepted

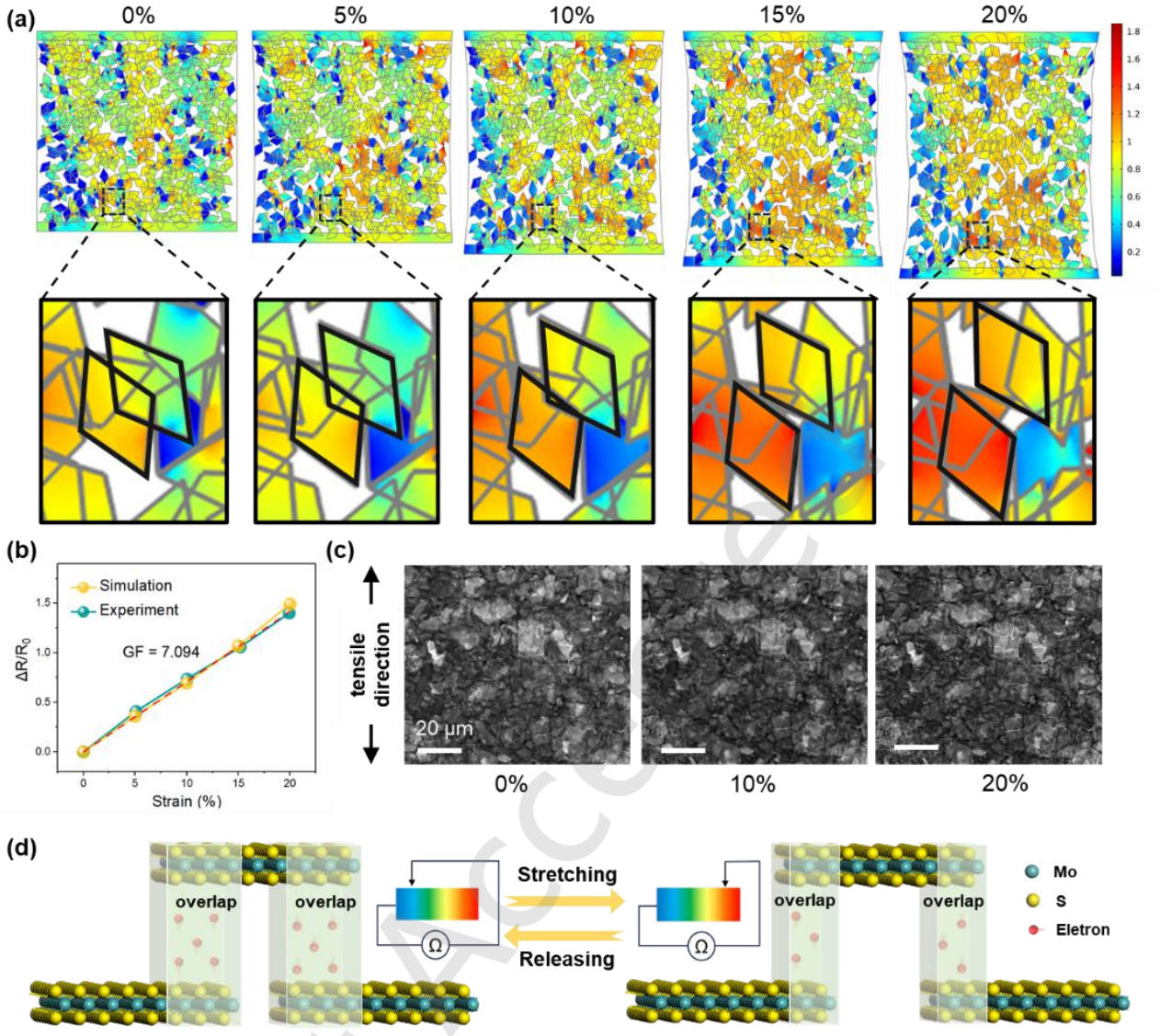

Figure 4 Sensing mechanism of the flexible strain sensor based on MoS_2 van der Waals films. (a) Finite element simulation analysis of current density distribution. (b) Relative resistance variation curves of simulation and experiment. (c) SEM images of the sensors under various strain: 0%, 10%, and 20%. (d) Schematic illustration of "Nanoscale Sliding Variable Resistor" model.

2.3 Sensing Mechanism Analysis

To clarify the relationship between the macroscopic performance and the microscopic structure of our flexible strain sensor, thereby deepening the understanding of its sensing mechanism, we performed finite element simulation analysis coupling electric field and solid mechanics field. Herein, we constructed a model representing layers of stacked MoS_2 nanosheets on PDMS substrate. Figure 4a shows the simulated current density distribution within the sensor model under tensile strains ranging from 0% to 20%. As the strain increases, local slip occurs between the nanosheets, reducing the overlapping area of adjacent nanosheets and consequently increasing the overall current density. Figure 4b presents the simulated relative resistance change ($\Delta R/R_0$) as a function of strain. The results show a linear increase in relative resistance with a constant gauge factor. The fitting curve agrees well with the experimental data, strongly supporting the premise that the response of our flexible strain sensor is governed by the interlayer sliding mechanism of the MoS_2 nanosheets. In situ SEM observations of the sensor surface under strains up to 20% (Figure 4c) reveal no discernible crack formation or propagation, thereby excluding crack-driven mechanisms and offering additional support for the interlayer sliding sensing mechanism.To visualize this mechanism, we conceptualize it as a "Nanoscale Sliding Variable Resistor" model (Figure 4d). When an external force stretches the PDMS substrate, the strong interfacial bonding between the substrate and the MoS_2 film effectively transfers the substrate deformation to the nanosheet layers. The stretching force is then transmitted layer-by-layer through the stacked nanosheets. The relatively weak van der Waals forces between adjacent nanosheets induce interlayer sliding upon stretching, reducing their overlapping area. Consequently, fewer electrons migrate across the nanosheet interfaces, which cause the interlayer contact resistance to increase. As this process occurs across multiple stacked nanosheet layers, the macroscopic resistance increases as well. Upon release of the external force, the nanosheets reversibly slide back to their initial positions so that good interlayer contact is restored and the resistance returns to its original state. This "Nanoscale Sliding Variable Resistor" mechanism leverages changes in the microscopic conductive pathway contact area to achieve a highly reversible electrical

response in the macroscopic resistance signal of the thin film.

It should be noted that the present analyses focus on the linear sensing range, where interlayer sliding between MoS_2 nanosheets remains reversible. Beyond this range, excessive strain may lead to irreversible nanosheet slippage, interfacial delamination, or crack formation, resulting in a pronounced increase in resistance. Such failure behaviors are beyond the scope of the current study and will be investigated in future work.

2.4 Application in Soft Mechanical Systems

To demonstrate practical applicability, the strain sensor was integrated onto a two-finger flexible gripper as a representative soft mechanical system. Figure 5a presents the overall circuit schematic of the actuated flexible gripper system. The electrical signals from the strain sensor are collected by the electrochemical workstation. The stepper motor is installed at the bottom of the flexible gripper and is controlled and adjusted by the motor driver connected to the microcontroller, allowing precise adjustment of the gripping motion. The gripping angle of the gripper can be controlled by adjusting the step distance of the screw. Figure 5b shows photographs of the flexible gripper. The flexible strain sensor is firmly fixed on the outer surface of the two-finger electrically driven gripper. As illustrated in the right image, bending deformation occurs during object grasping, during which the sensor undergoes tensile strain synchronously with the gripper fingers.

Based on this configuration, an intelligent closed-loop grasping system capable of discriminating grasping states and identifying objects of different sizes was developed, as schematically illustrated in Figure 5c. The grasping process starts with the gripper opening to a predefined angle to ensure object enclosure, followed by grasping and lifting using a small closing angle (i.e., step distance). During this process, the strain sensor monitors gripper deformation in real time and outputs electrical signals for analysis. If the resistance signal rises to a peak and subsequently exhibits pronounced fluctuations followed by a continuous decrease, the grasping event is identified as slipping. In this case, the gripper returns to its initial open state and applies a larger closing angle for a new grasping attempt. In contrast, if the resistance signal rises to a peak and remains nearly stable, the grasp is identified as stable, and the object is held in a lifted state, completing the grasping cycle. To achieve this objective, the strain sensor is required to exhibit high linearity, low hysteresis, and stable signal output under cyclic deformation, since ambiguous or delayed signal responses may lead to incorrect grasping decisions. The strain sensor developed in our work satisfies these requirements, thereby enabling robust grasping-state discrimination and size perception in the proposed system.

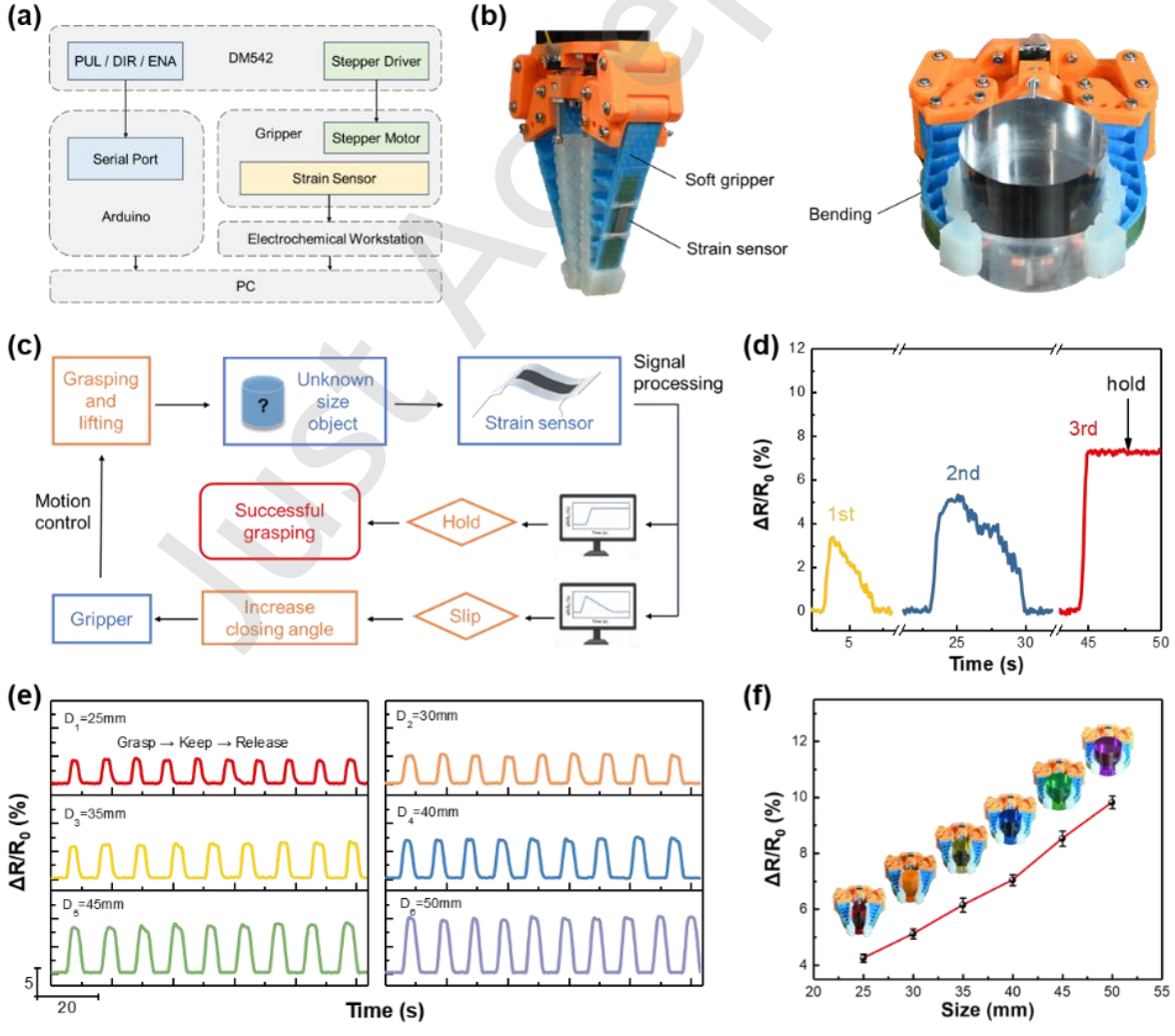

Figure 5 Application of the strain sensor in a flexible gripper system. (a) Circuit schematic of the flexible gripper and signal acquisition system. (b) Photographs of the two-finger flexible gripper integrated with the strain sensor. (c) Workflow diagram of the intelligent closed-loop grasping system based on

Just Accepted

strain sensing. (d) Resistance response during repeated grasping of the same object. (e) Relative resistance responses during repeated grasping and releasing of cylindrical objects with different diameters. (f) Peak relative resistance changes extracted from multiple grasping cycles for objects of different sizes.

Movie S1 shows three consecutive grasping attempts of the same object. The first two attempts result in slipping, which is identified by pronounced resistance fluctuations exceeding the baseline noise level followed by a continuous and monotonic decrease in resistance, indicating relative motion between the gripper and the object. In contrast, during the third attempt, the resistance signal remains stable after reaching its peak, indicating successful and stable grasping (Figure 5d). Under the condition that stable grasping is ensured, the gripper was operated with identical opening and closing angles to identify objects of different sizes. Figure 5f shows the resistance responses during grasping of cylindrical objects with different diameters (25 mm, 30 mm, 35 mm, 40 mm, 45 mm and 50 mm). The resistance variations remain highly consistent over multiple grasping–releasing cycles, demonstrating good repeatability. Based on the peak resistance changes extracted from ten grasping events, Figure 5e reveals that the strain sensor can clearly distinguish object sizes through deformation-induced resistance variations, even without explicit visual or geometric feedback.

Such repeatable resistance responses based on strain sensing show strong potential for applications in soft robotic manipulation, such as adaptive gripping of fragile objects, sorting based on size perception and human–robot interaction tasks. In particular, the ability to infer grasping stability and object size from deformation feedback makes the proposed sensor well suited for soft machines operating in complex environments and uncertain object properties. Benefiting from the crack-free MoS_2 van der Waals film and the interlayer sliding–dominated sensing mechanism, the sensor presented in this work shows a highly linear and stable electrical response under repeated deformation. This feature effectively reduces signal fluctuation and drift during practical operation, which is critical for reliable motion monitoring and closed-loop control applications. In addition, the outstanding cycling durability ensures consistent performance during long-term use, highlighting the strong potential of this sensor for practical flexible and wearable systems.

3 Conclusions

In this study, we developed a flexible strain sensor based on MoS_2 van der Waals films, which exhibits a rare combination of high linearity, low hysteresis, and outstanding durability under cyclic deformation. Enabled by reversible interlayer sliding and robust interfacial bonding with PDMS, the sensor maintains stable electrical performance over more than 40,000 cycles, effectively mitigating fatigue-induced degradation commonly observed in crack-based sensing mechanisms. Using a flexible gripper as a representative soft mechanical system, the practical sensing capability of the device is demonstrated. This work establishes interlayer sliding as an effective design principle for durable flexible strain sensors and suggests promising opportunities for their application in advanced soft machines and deformable electronic systems.

4 Experimental Section

4.1 Materials

Molybdenum disulfide (MoS_2, single crystal) was purchased from SixCarbon Technology Shenzhen. Tetraheptylammonium bromide (THAB), acetonitrile (ACN), polyvinylpyrrolidone (PVP), N,N-dimethylformamide (DMF), and isopropyl alcohol (IPA) were obtained from commercial suppliers and used as received. Polydimethylsiloxane (PDMS, Sylgard 184) was purchased from Dow Corning.

4.2 Synthesis of MoS_2 Nanosheets

MoS_2 nanosheets were prepared via electrochemical intercalation exfoliation followed by liquid cascade centrifugation. Briefly, 150 mg of THAB was dissolved in 30 mL of acetonitrile to serve as the electrolyte. A MoS_2 single crystal was used as the cathode and graphite as the anode. An intercalation voltage of −8 V was applied for 2 h. The intercalated crystals were transferred into a PVP/DMF solution and ultrasonicated for 5–30 min. The resulting dispersion was centrifuged and repeatedly washed with IPA to obtain uniformly dispersed MoS_2 nanosheets.

4.3 Deposition of MoS_2 Films

A defined volume of MoS_2 nanosheet dispersion with a concentration of 0.1 mg mL^{-1} was vacuum-filtered to form a conductive MoS_2 film. The film was cut into rectangular strips (0.5 cm × 1.5 cm) and subjected to oxygen plasma surface treatment at 50 W for 5 s to enhance surface reactivity.

4.4 Fabrication of Strain Sensors

PDMS prepolymer and curing agent were mixed at a mass ratio of 10:1 and degassed under vacuum. The mixture was partially cured at 80 °C for 15 min to obtain a tacky surface. The plasma-treated MoS_2 film was laminated onto the pre-cured PDMS and further cured at 80 °C for 1 h. After demolding, electrical leads were attached to both ends of the MoS_2 film using silver paste and encapsulated with silicone rubber to complete the fabrication of the flexible strain sensor.

4.5 Characterization and Measurements

The crystal phase structure of the nanosheets was characterized using a field-emission transmission electron microscope (FE-TEM, Tecnai G2 F20, FEI Electron Optics, Netherlands). The morphology of the nanosheets and the films was examined by field-emission scanning electron microscopy (FE-SEM, SU8200, Hitachi, Japan) and atomic force microscopy (AFM, NTEGRA, NT-MDT, Russia). The concentration of the nanosheet dispersions was determined using a UV–visible spectrophotometer (Lambda 1050, PerkinElmer, USA). The elemental composition and chemical states of the films were analyzed by X-ray photoelectron spectroscopy (XPS, K-Alpha, Thermo Scientific, USA). The interlayer spacing of the films was measured using an X-ray diffractometer (XRD, D8 DISCOVER DAVINCI, Bruker AXS GmbH, Germany). The electrical properties of the films were evaluated using a Hall measurement system (Accent HL5500). The resistance variation of the devices was measured using a portable precision resistance/capacitance meter (True Box RC01, LinkZill, China) and an electrochemical workstation (PGSTAT302N, Autolab, Switzerland).

Electronic Supplementary Material: Supplementary material

Just Accepted

(Manufacturing process and supplementary characterization data of MoS_2 van der Waals film strain sensors) is available in the online version of this article at https://doi.org/10.26599/NR.2026.94908860.

Data availability

All data needed to support the conclusions in the paper are presented in the manuscript and the Electronic Supplementary Material. Additional data related to this paper may be requested from the corresponding author upon request.

Acknowledgements

This work was financially supported by the National Key Research and Development Program of China (Grant No. 2024YFB3814100), National Natural Science Foundation of China (62471459, U24A20228 and 62301540), the Chinese Academy of Sciences Project for Young Scientists in Basic Research (Grant No.YSBR-109), Joint Project "ActFiber-FFG/CAS: 931688/030GJHZ2025029MI" managed by Austrian Research Promotion Agency (FFG) and Chinese Academy of Sciences (CAS).

Declaration of competing interest

All the contributing authors report no conflict of interests in this work.

Author contribution statement

X. X. Z.: Data curation, formal analysis, investigation, methodology, project administration, validation, visualization, writing – original draft. H. O.: Data curation, methodology, software. L. J. S.: Funding acquisition, project administration, supervision. Y. C.: Funding acquisition, project administration, supervision. J. S.: Funding acquisition, project administration, supervision. R. R. W.: Conceptualization, funding acquisition, methodology, project administration, resources, supervision, writing – review & editing. All the authors have approved the final manuscript.

Use of AI statement

None.

References

[1] Liu, Z.; Hu, X.; Bo, R.; Yang, Y.; Cheng, X.; Pang, W.; Liu, Q.; Wang, Y.; Wang, S.; Xu, S.; Shen, Z.; Zhang, Y. A three-dimensionally architected electronic skin mimicking human mechanosensation. *Science* **2024**, *384*, 987-994.

[2] Zhou, J.; Zhang, Q.; Zhang, M.; Aikebaier, S.; Zhu, X.; Zhou, X. Flexible wearable medical devices: from material innovations and data processing to intelligent healthcare applications. *Journal of Advanced Research* **2025**, https://doi.org/10.1016/j.jare.2025.08.036.

[3] Chen, X.; Wang, C.; Wei, W.; Liu, Y.; Ge, S. S.; Zhou, L.; Kong, H. Flexible and sensitive pressure sensor with enhanced breathability for advanced wearable health monitoring. *npj Flexible Electronics* **2025**, *9*, 101.

[4] Sun, G.; Ma, Z.; Xiao, Z.; Meng, L.; Liu, Z.; Wang, P.; Zhang, Z.; Li, Z.; Meng, C.; Guo, S. All-Fiber-Type Temperature Sensor Powered by Zinc-Ion Battery toward Wearable Sensing Clothes for Health Monitoring. *Advanced Functional Materials* **2026**, *36*, e18490.

[5] Sun, G.; Wang, D.; Wang, P.; Meng, Y.; Fu, X.; Yan, H.; Meng, C. A Flexible Temperature Sensor with Ultrafast Response Speed and High Stability Achieved by Improving Substrate Thermal Conductivity and Radiative Cooling. *Advanced Functional Materials* **2026**, *36*, e12296.

[6] Li, J.; Zhao, Y.; Fan, Y.; Chen, J.; Gong, J.; Li, W. J. Flexible wearable electronics for enhanced human-computer interaction and virtual reality applications. *Nano Energy* **2025**, *138*, 110821.

[7] Xu, C.; Chen, J.; Zhu, Z.; Liu, M.; Lan, R.; Chen, X.; Tang, W.; Zhang, Y.; Li, H. Flexible Pressure Sensors in Human–Machine Interface Applications. *Small* **2024**, *20*, 2306655.

[8] An, X.; Niu, S.; Chen, J.; Zhang, X.; Zhang, J.; Liu, T.; Duan, Z.; Hu, Y.; Qi, D.; Zhang, J.; Chen, X. Flexible Electronics in Robotics Systems: From Devices to Applications. *SmartBot*, *n/a*, e70017.

[9] Sun, G.; Sun, Z.; Liu, L.; Wang, P.; Zhang, Z.; Li, Z.; Meng, C.; Guo, S. Transparent Conductive Hydrogels with Water-Responsive Contractility, Repairability, and Biocompatibility for Visible Conformal Shape-Adaptive Tissue-Adherent Monitoring. *Advanced Functional Materials* **2026**, *36*, e22718.

[10] Li, J.; Yao, Z.; Meng, X.; Zhang, X.; Wang, Z.; Wang, J.; Ma, G.; Liu, L.; Zhang, J.; Niu, S.; Han, Z.; Ren, L. High-Fidelity, Low-Hysteresis Bionic Flexible Strain Sensors for Soft Machines. *ACS Nano* **2024**, *18*, 2520-2530.

[11] Yang, H.; Ding, S.; Wang, J.; Sun, S.; Swaminathan, R.; Ng, S. W. L.; Pan, X.; Ho, G. W. Computational design of ultra-robust strain sensors for soft robot perception and autonomy. *Nature Communications* **2024**, *15*, 1636.

[12] Liu, H.; Takakuwa, M.; Yamamoto, M.; Nakashima, S.; Jiang, Z.; Yokota, T.; Someya, T.; Itoh, T.; Takamatsu, S. Ultrathin bending sensor with ultrahigh robustness and reliability for robotic applications. *npj Flexible Electronics* **2025**, *9*, 123.

[13] Xue, F.; Peng, Q.; Ding, R.; Li, P.; Zhao, X.; Zheng, H.; Xu, L.; Tang, Z.; Zhang, X.; He, X. Ultra-sensitive, highly linear, and hysteresis-free strain sensors enabled by gradient stiffness sliding strategy. *npj Flexible Electronics* **2024**, *8*, 14.

[14] Zhao, S.; Liu, D.; Yan, F. Wearable Resistive-Type Stretchable Strain Sensors: Materials and Applications. *Advanced Materials* **2025**, *37*, 2413929.

[15] Li, M.; Hu, Z.; Yan, B.; Wang, J.; Zhang, H.; Ye, F.; Sun, B.; Liu, J.; Li, Y.; Ding, G.; Zang, F.; Yang, Z. A flexible resistive strain gauge with reduced temperature effect via thermal expansion anisotropic composite substrate. *Microsystems & Nanoengineering* **2024**, *10*, 129.

[16] Li, S.; Yu, Y.; Wu, Y.; Li, Y.; Tang, M.; Wei, K.; Shang, J.; Liu, Y.; Wang, H.; Li, R.-W. Advances in flexible resistive strain sensors and their applications. *Materials Today Communications* **2025**, *49*, 113975.

[17] He, R.; Yang, P. Giant piezoresistance effect in silicon nanowires. *Nature Nanotechnology* **2006**, *1*, 42-46.

[18] Pan, Q.; Lu, L. Fatigue in metals and alloys. *Nature Materials* **2025**, 10.1038/s41563-025-02308-5.

[19] Paul, S. J.; Elizabeth, I.; Gupta, B. K. Ultrasensitive Wearable Strain Sensors based on a VACNT/PDMS Thin Film for a Wide Range of Human Motion Monitoring. *ACS Applied Materials & Interfaces* **2021**, *13*, 8871-8879.

[20] Zhao, Y.; Shen, T.; Zhang, M.; Yin, R.; Zheng, Y.; Liu, H.; Sun, H.; Liu, C.; Shen, C. Advancing the pressure sensing performance of conductive CNT/PDMS composite film by constructing a hierarchical-structured surface. *Nano Materials Science* **2023**, *5*, 343-350.

[21] Lu, Y.; Yang, G.; Wang, S.; Zhang, Y.; Jian, Y.; He, L.; Yu, T.; Luo, H.; Kong, D.; Xianyu, Y.; Liang, B.; Liu, T.; Ouyang, X.; Yu, J.; Hu, X.; Yang, H.; Gu, Z.; Huang, W.; Xu, K. Stretchable graphene–hydrogel interfaces for wearable and implantable bioelectronics. *Nature Electronics* **2024**, *7*, 51-65.

[22] Gao, Y.; Sun, J.; Tian, X.; Yuan, Y. Ultra-highly sensitive graphene/polyaniline@epoxidized natural rubber strain sensors for human motion monitoring. *Sensors and Actuators A: Physical* **2023**, *358*, 114421.

[23] Yang, X.; Gui, J.; Dong, C.; Zhao, J.; Xu, R. Laser-Induced

Just Accepted

Graphene for Screen-Printed Strain Sensors. *ACS Applied Nano Materials* **2023**, *6*, 21679-21687.
[24] Chen, H.; Zhuo, F.; Zhou, J.; Liu, Y.; Zhang, J.; Dong, S.; Liu, X.; Elmarakbi, A.; Duan, H.; Fu, Y. Advances in graphene-based flexible and wearable strain sensors. *Chemical Engineering Journal* **2023**, *464*, 142576.
[25] Yang, Y.; Shi, L.; Cao, Z.; Wang, R.; Sun, J. Strain Sensors with a High Sensitivity and a Wide Sensing Range Based on a Ti3C2Tx (MXene) Nanoparticle–Nanosheet Hybrid Network. *Advanced Functional Materials* **2019**, *29*, 1807882.
[26] Duan, Z.; Yuan, M.; Liu, Z.; Pei, W.; Jiang, K.; Li, L.; Shen, G. An Ultrasensitive Ti3C2Tx MXene-based Soft Contact Lens for Continuous and Nondestructive Intraocular Pressure Monitoring. *Small* **2024**, *20*, 2309785.
[27] Pei, Y.; Zhang, X.; Hui, Z.; Zhou, J.; Huang, X.; Sun, G.; Huang, W. Ti3C2TX MXene for Sensing Applications: Recent Progress, Design Principles, and Future Perspectives. *ACS Nano* **2021**, *15*, 3996-4017.
[28] Gong, S.; Zhang, X.; Nguyen, X. A.; Shi, Q.; Lin, F.; Chauhan, S.; Ge, Z.; Cheng, W. Hierarchically resistive skins as specific and multimetric on-throat wearable biosensors. *Nature Nanotechnology* **2023**, *18*, 889-897.
[29] Xu, F.; Zhu, Y. Highly Conductive and Stretchable Silver Nanowire Conductors. *Advanced Materials* **2012**, *24*, 5117-5122.
[30] Lee, C.-J.; Park, K. H.; Han, C. J.; Oh, M. S.; You, B.; Kim, Y.-S.; Kim, J.-W. Crack-induced Ag nanowire networks for transparent, stretchable, and highly sensitive strain sensors. *Scientific Reports* **2017**, *7*, 7959.
[31] Gul, O.; Song, M.; Gu, C.-Y.; Ahn, J.; Lee, K.; Ahn, J.; Kim, H. J.; Kim, T.-S.; Park, I. Bioinspired interfacial engineering for highly stretchable electronics. *Nature Communications* **2025**, *16*, 1337.
[32] Lee, D. H.; Miyashita, T.; Xuan, Y.; Takei, K. Ultrasensitive and Stretchable Strain Sensors Based on Laser-Induced Graphene With ZnO Nanoparticles. *ACS Nano* **2024**, *18*, 32255-32265.
[33] Liu, Y.; Xu, Z.; Ji, X.; Xu, X.; Chen, F.; Pan, X.; Fu, Z.; Chen, Y.; Zhang, Z.; Liu, H.; Cheng, B.; Liang, J. Ag–thiolate interactions to enable an ultrasensitive and stretchable MXene strain sensor with high temporospatial resolution. *Nature Communications* **2024**, *15*, 5354.
[34] Sun, H.; Fang, X.; Fang, Z.; Zhao, L.; Tian, B.; Verma, P.; Maeda, R.; Jiang, Z. An ultrasensitive and stretchable strain sensor based on a microcrack structure for motion monitoring. *Microsystems & Nanoengineering* **2022**, *8*, 111.
[35] Yang, T.; Jiang, X.; Huang, Y.; Tian, Q.; Zhang, L.; Dai, Z.; Zhu, H. Mechanical sensors based on two-dimensional materials: Sensing mechanisms, structural designs and wearable applications. *iScience* **2022**, *25*, 103728.
[36] Ren, J.; Zhang, W.; Wang, Y.; Wang, Y.; Zhou, J.; Dai, L.; Xu, M. A graphene rheostat for highly durable and stretchable strain sensor. *InfoMat* **2019**, *1*, 396-406.
[37] Li, S.; Liu, G.; Li, R.; Li, Q.; Zhao, Y.; Huang, M.; Zhang, M.; Yin, S.; Zhou, Y.; Tang, H.; Wang, L.; Fang, G.; Su, Y. Contact-Resistance-Free Stretchable Strain Sensors with High Repeatability and Linearity. *ACS Nano* **2022**, *16*, 541-553.
[38] Gao, Z.; Wei, T.-R.; Deng, T.; Qiu, P.; Xu, W.; Wang, Y.; Chen, L.; Shi, X. High-throughput screening of 2D van der Waals crystals with plastic deformability. *Nature Communications* **2022**, *13*, 7491.
[39] Deng, T.; Gao, Z.; Li, Z.; Qiu, P.; Li, Z.; Yuan, X.; Ming, C.; Wei, T.-R.; Chen, L.; Shi, X. Room-temperature exceptional plasticity in defective Bi₂Te₃-based bulk thermoelectric crystals. *Science* **2024**, *386*, 1112-1117.
[40] Schrenker, N. J.; Xie, Z.; Schweizer, P.; Moninger, M.; Werner, F.; Karpstein, N.; Mačković, M.; Spyropoulos, G. D.; Göbelt, M.; Christiansen, S.; Brabec, C. J.; Bitzek, E.; Spiecker, E. Microscopic Deformation Modes and Impact of Network Anisotropy on the Mechanical and Electrical Performance of Five-fold Twinned Silver Nanowire Electrodes. *ACS Nano* **2021**, *15*, 362-376.
[41] Yan, W.; Fuh, H.-R.; Lv, Y.; Chen, K.-Q.; Tsai, T.-Y.; Wu, Y.-R.; Shieh, T.-H.; Hung, K.-M.; Li, J.; Zhang, D.; Ó Coileáin, C.; Arora, S. K.; Wang, Z.; Jiang, Z.; Chang, C.-R.; Wu, H.-C. Giant gauge factor of Van der Waals material based strain sensors. *Nature Communications* **2021**, *12*, 2018.
[42] Li, Z.; Chen, Y.; Liu, S.; Li, W.; Liu, L.; Song, W.; Lu, D.; Ma, L.; Yang, X.; Xie, Z.; Duan, X.; Yang, Z.; Wang, Y.; Liao, L.; Liu, Y. Strain Releasing of Flexible 2D Electronics through van der Waals Sliding Contact. *ACS Nano* **2022**, *16*, 13152-13159.
[43] Lin, Z.; Liu, Y.; Halim, U.; Ding, M.; Liu, Y.; Wang, Y.; Jia, C.; Chen, P.; Duan, X.; Wang, C.; Song, F.; Li, M.; Wan, C.; Huang, Y.; Duan, X. Solution-processable 2D semiconductors for high-performance large-area electronics. *Nature* **2018**, *562*, 254-258.
[44] Liao, L.; Kovalska, E.; Regner, J.; Song, Q.; Sofer, Z. Two-Dimensional Van Der Waals Thin Film and Device. *Small* **2024**, *20*, 2303638.
[45] Wang, Y.; Wang, F.; Yazigi, S.; Zhang, D.; Gui, X.; Qi, Y.; Zhong, J.; Sun, L. Nanoengineered highly sensitive and stable soft strain sensor built from cracked carbon nanotube network/composite bilayers. *Carbon* **2021**, *173*, 849-856.
[46] Wang, Y.; Qin, W.; Yang, M.; Tian, Z.; Guo, W.; Sun, J.; Zhou, X.; Fei, B.; An, B.; Sun, R.; Yin, S.; Liu, Z. High Linearity, Low Hysteresis Ti3C2Tx MXene/AgNW/Liquid Metal Self-Healing Strain Sensor Modulated by Dynamic Disulfide and Hydrogen Bonds. *Advanced Functional Materials* **2023**, *33*, 2301587.
[47] Liu, B.; Lan, B.; Shi, L.; Cheng, Y.; Sun, J.; Wang, R. Batch Fabrication of Flexible Strain Sensors with High Linearity and Low Hysteresis for Health Monitoring and Motion Detection. *ACS Applied Materials & Interfaces* **2024**, *16*, 36821-36831.
[48] Yang, S.; Ling, Y.; Wu, Q.; Zhang, H.; Yan, Z.; Huang, G.; Lin, J.; Wan, C. Lignin-derived porous graphene for wearable and ultrasensitive strain sensors. *Journal of Materials Chemistry C* **2022**, *10*, 11730-11738.
[49] Zhang, Y.; Liu, J.; Pan, Y.; Luo, K.; Yu, J.; Zhang, Y.; Jia, K.; Yin, H.; Zhu, H.; Tian, H.; Wu, Z. The evolution of MoS2 properties under oxygen plasma treatment and its application in MoS2 based devices. *Journal of Materials Science: Materials in Electronics* **2019**, *30*, 18185-18190.
[50] Luo, Y.; Fan, H.; Lai, X.; Zeng, Z. a.; Lan, X.; Lin, P.; Tang, L.; Wang, W.; Chen, Y.; Tang, Y. Flexible liquid metal-based microfluidic strain sensors with fractal-designed microchannels for monitoring human motion and physiological signals. *Biosensors and Bioelectronics* **2024**, *246*, 115905.
[51] Ko, S.; Chhetry, A.; Kim, D.; Yoon, H.; Park, J. Y. Hysteresis-Free Double-Network Hydrogel-Based Strain Sensor for Wearable Smart Bioelectronics. *ACS Applied Materials & Interfaces* **2022**, *14*, 31363-31372.
[52] Park, T.; Woo, H. K.; Jung, B. K.; Park, B.; Bang, J.; Kim, W.; Jeon, S.; Ahn, J.; Lee, Y.; Lee, Y. M.; Kim, T.-i.; Oh, S. J. Noninterference Wearable Strain Sensor: Near-Zero Temperature Coefficient of Resistance Nanoparticle Arrays with Thermal Expansion and Transport Engineering. *ACS Nano* **2021**, *15*, 8120-8129.

© The Author(s) 2026. *Nano Research* published by Tsinghua University Press. The articles published in this open access journal are distributed under the terms of the Creative Commons Attribution 4.0 International License (http://creativecommons.org/licenses/by/4.0/), which permits use, distribution and reproduction in any medium, provided the original work is properly cited.

Just Accepted

Electronic Supplementary Material

A highly linear and durable flexible strain sensor based on MoS_2 van der Waals films for soft machines

Xiangxu Zhu[1,2], Hao Ouyang[1,2], Liangjing Shi[1], Yin Cheng[1], Jing Sun[1], and Ranran Wang [1,3]

[1] *The State Key Laboratory of High Performance Ceramics, Shanghai Institute of Ceramics, Chinese Academy of Sciences, Shanghai 200050, China*
[2] *Center of Materials Science and Optoelectronics Engineering, University of Chinese Academy of Sciences, Beijing 100049, China*
[3] *School of Chemistry and Materials Science, Hangzhou Institute for Advanced Study, University of Chinese Academy of Sciences, Hangzhou 310024, China*

Supporting information to https://doi.org/10.26599/NR.2026.94908860

Just Accepted

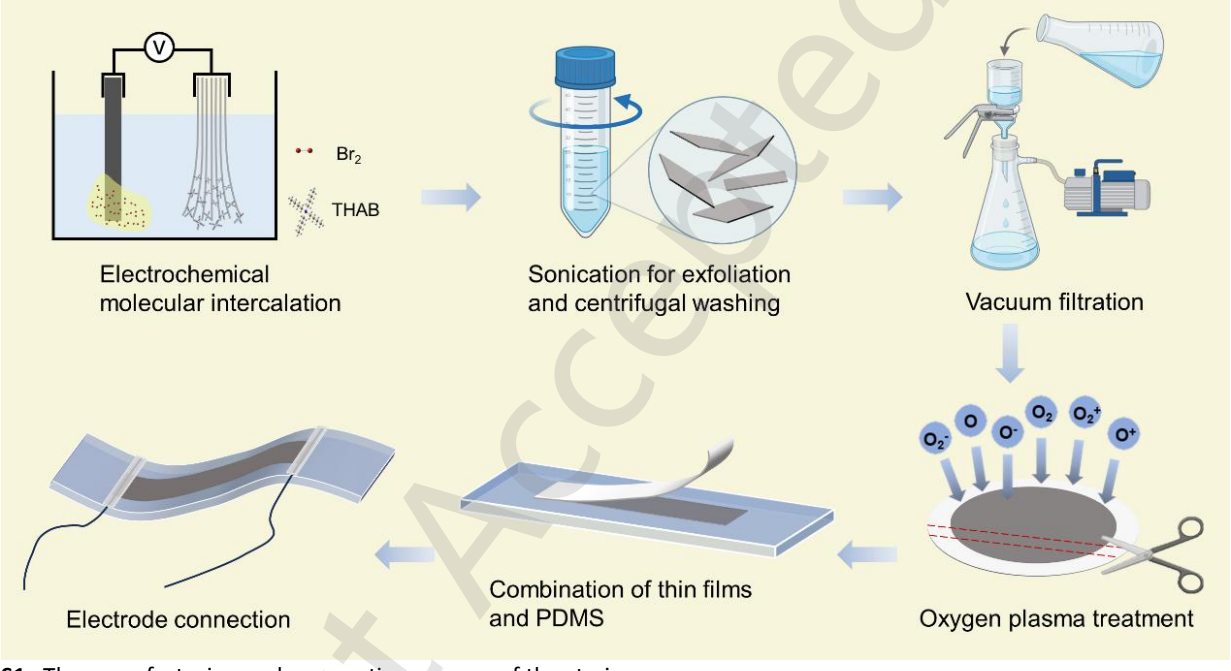

Figure S1 The manufacturing and preparation process of the strain sensor.

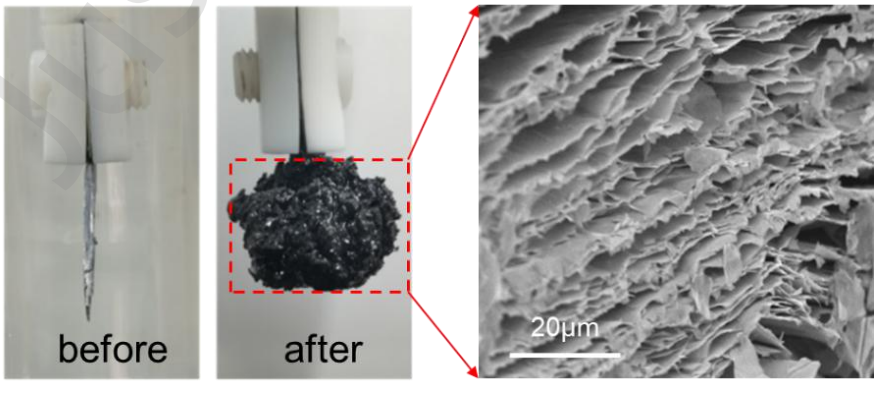

Figure S2 Photos of MoS_2 crystal before and after intercalation.

Address correspondence to wangranran@mail.sic.ac.cn

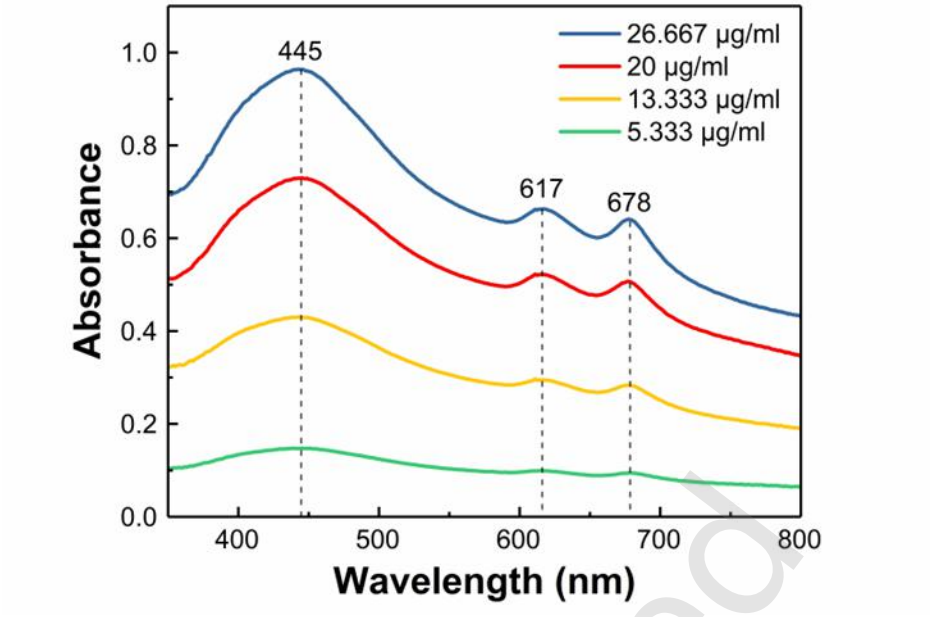

Figure S3 UV–vis absorption of MoS_2 nanosheet dispersion solutions with different concentrations.

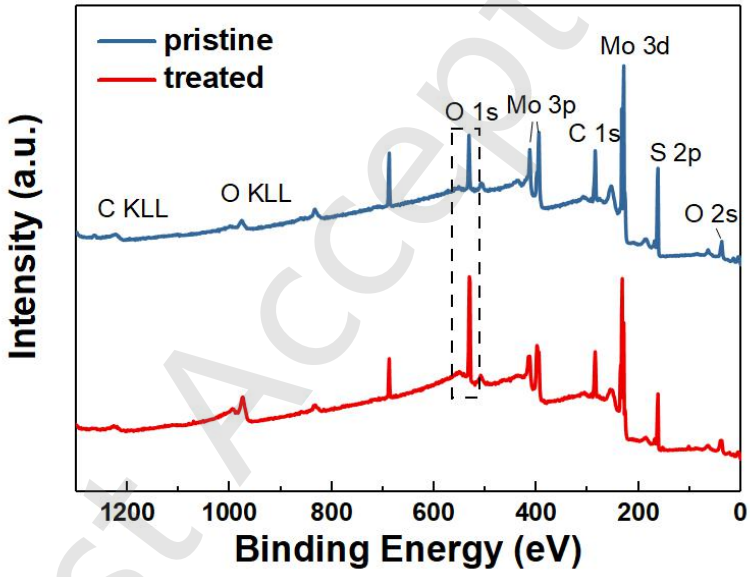

Figure S4 XPS spectra and elemental analysis comparing pristine and plasma-treated MoS_2.

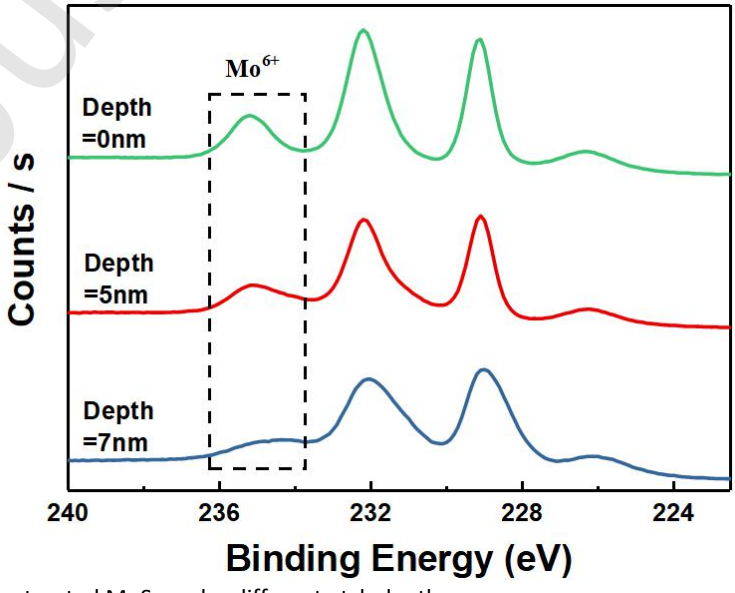

Figure S5 XPS spectra of plasma-treated MoS_2 under different etch depth.

Just Accepted

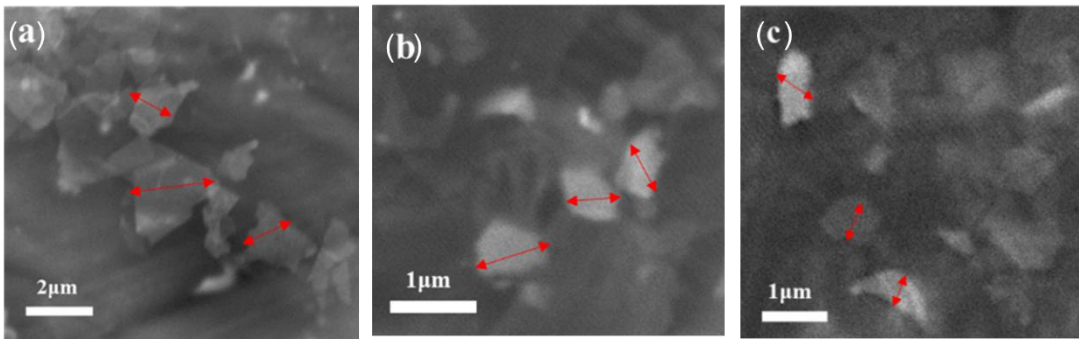

Figure S6 The lateral size of (a) d_{5min}-c_{1-3k}-MoS_2 nanosheets (~1.55 μm), (b) d_{10min}-c_{3-5k}-MoS_2 nanosheets (~0.80 μm), and (c) d_{30min}-c_{5-8k}-MoS_2 nanosheets (~0.52 μm).

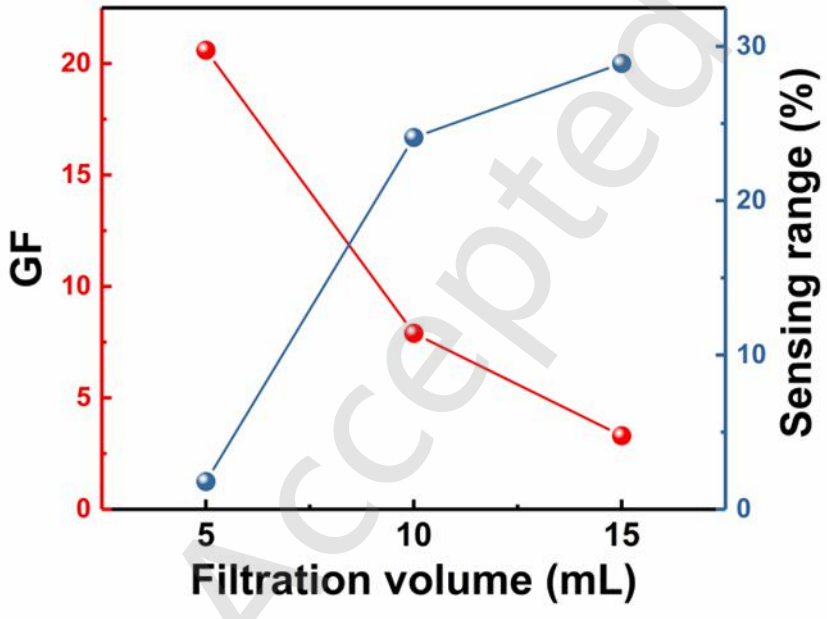

Figure S7 Dependence of gauge factor (left axis) and linear sensing range (right axis) on the filtration volume at a fixed concentration, reflecting the relative thickness of MoS_2 films.

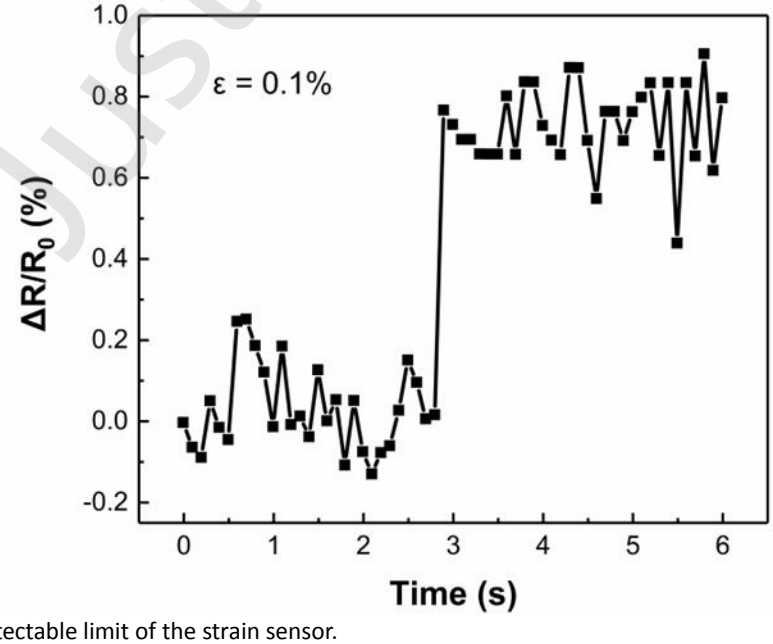

Figure S8 Minimum detectable limit of the strain sensor.

Just Accepted

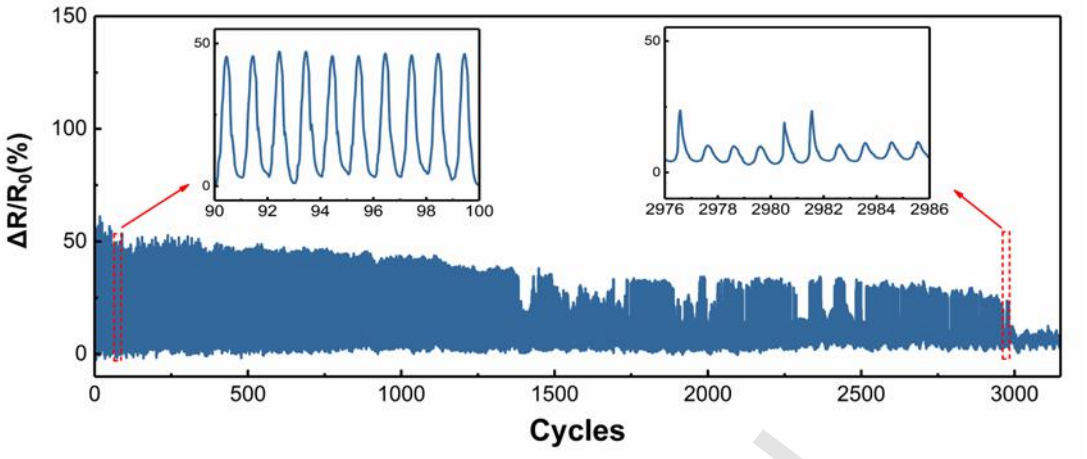

Figure S9 Minimum detectable limit of the strain sensor.

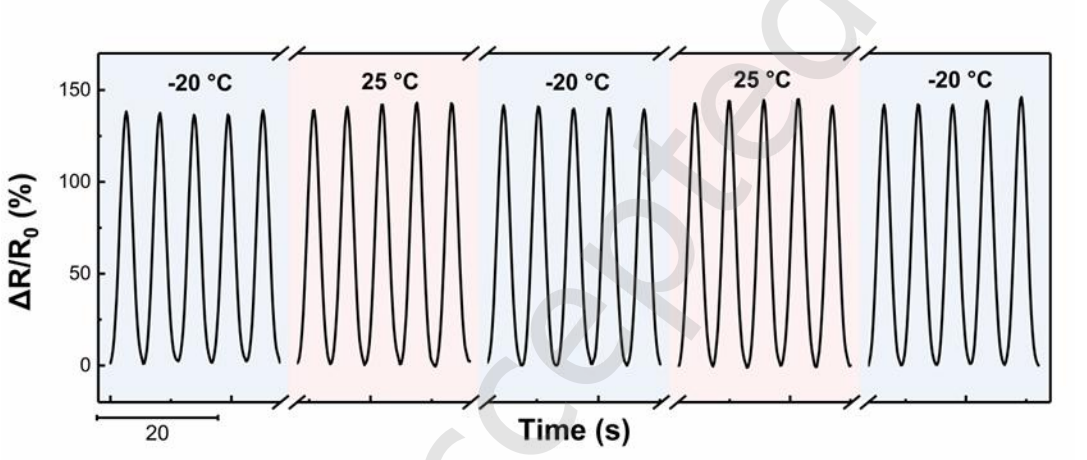

Figure S10 Temperature cycling response of the strain sensor during repeated switching between −20 °C and 25 °C (ε = 20%).

Table S1 Performance comparison of the MoS_2 flexible strain sensor in this work with representative flexible strain sensors reported in the literature.

Materials	Gauge factor	Sensing range	R^2	Hysteresis	Repeatability (cycles)	References
Constantan/PI/Ecoflex	20	60%	N/A	2.9%	1200*	[10]
Au/CNT/PDMS	0.0052	50%	0.999	0.3%	20000	[37]
CNT/PDMS	207	50%	0.93	N/A	10000	[45]
$Ti_3C_2T_x$ MXene/AgNW/liquid metal	3.22	300%	0.98157	0.448%	1000	[46]
CNT/TPU	60	50%	0.997	5%	10000	[47]
Lignin-derived porous graphene	960	14%	0.99	7%	10000	[48]
MoS_2/PDMS	40.87	30%	0.999	2.1%	40000	This work

* Calculated from the reported loading–unloading frequency (1 Hz) and cycling duration (20 min).

Just Accepted